Title

Ultrasensitive and multiplexed tracking of single cells using whole-body PET/CT.

Journal

Science Advances, 10(24)

Authors

Nguyen, Hieu

Das, Neeladrisingha

Ricks, Matthew

et al.

Publication Date

2024-06-14

DOI

10.1126/sciadv.adk5747

APPLIED SCIENCES AND ENGINEERING

Ultrasensitive and multiplexed tracking of single cells using whole-body PET/CT

Hieu T. M. Nguyen[1], Neeladrisingha Das[1], Matthew Ricks[2], Xiaoxu Zhong[1], Eri Takematsu[3], Yuting Wang[3], Carlos Ruvalcaba[4], Brahim Mehadji[5], Emilie Roncali[4,5], Charles K. F. Chan[3]†, Guillem Pratx[1]*

In vivo molecular imaging tools are crucially important for elucidating how cells move through complex biological systems; however, achieving single-cell sensitivity over the entire body remains challenging. Here, we report a highly sensitive and multiplexed approach for tracking upward of 20 single cells simultaneously in the same subject using positron emission tomography (PET). The method relies on a statistical tracking algorithm (PEPT-EM) to achieve a sensitivity of 4 becquerel per cell and a streamlined workflow to reliably label single cells with over 50 becquerel per cell of ^{18}F-fluorodeoxyglucose (FDG). To demonstrate the potential of the method, we tracked the fate of more than 70 melanoma cells after intracardiac injection and found they primarily arrested in the small capillaries of the pulmonary, musculoskeletal, and digestive organ systems. This study bolsters the evolving potential of PET in offering unmatched insights into the earliest phases of cell trafficking in physiological and pathological processes and in cell-based therapies.

INTRODUCTION

Over the past decades, considerable progress has been made in the field of molecular imaging to develop techniques specifically aimed at tracking the movement of cells inside the body. These techniques have found application in a range of different biological fields, where they have been used to characterize the spread of tumor cells and subsequent formation of metastases (*1*), the spatial kinetics of immune cells in response to pathogens (*2*, *3*), the migration of regenerative stem cells toward damaged tissues (*4*–*6*), and other key biological processes such as embryonic development and immune cell patrolling (*7*, *8*). These imaging tools have become crucial for monitoring the fate of cells as they move across the body and understanding the role that this migration plays in the context of physiological and pathological processes and cell-based therapies.

Positron emission tomography (PET), known for its exceptional sensitivity across the entire body, offers a compelling platform for tracking cellular dynamics in human subjects and preclinical animal models (*9*–*11*). However, applications of this technique have been predominantly conducted on a population level, which is incompatible with the need to elucidate the trajectories of individual cells. To address this limitation, we previously devised a methodology to expand the capabilities of PET into the realm of single-cell imaging. Using mesoporous silica nanoparticles (MSNs), we efficiently labeled cells with ^{68}Ga and visualized the migration and arrest of solitary breast cancer cells in lung capillaries (*12*). Cells containing upward of 27 becquerel (Bq) per cell produced sufficient signal to be clearly distinguished, and sensitivity was further improved by the use of a tracking algorithm called CellGPS (*12*–*14*). These results firmly established PET as an excellent method for tracking single cells across the body.

However, the promise that PET holds for tracking single cells can only be realized once remaining challenges have been addressed. Foremost among these is the lack of cellular multiplexing capabilities in the initial implementation of this technique, which could track just one cell per animal. Because of this low throughput, larger studies involving 10 or more cells were prohibitive to conduct. Second, despite its high efficiency, the cell labeling workflow based on MSNs proved laborious and at times inconsistent due to its complexity and lack of automation. This limitation became particularly restrictive as we sought to deploy the technique on a more routine basis to study the fate of cancer cells during metastasis. Third, a more fundamental question arose concerning the lower limit of detection achievable with PET. While we could previously image single cells containing around 20 Bq, theoretical considerations suggest that the detection threshold could be lowered even further, which would have implications for tracking different types of cells and for improving the temporal resolution.

We here report a multiplexed approach for tracking upward of 20 cancer cells concurrently in the same subject using PET. The proposed workflow represents a considerable improvement in nearly every aspect, including cell labeling, single-cell dispensing, data acquisition, data reconstruction, and disease modeling. In addition to the 20-fold improvement in multiplexing capability, we demonstrate a detection threshold of 4 Bq for single cells, representing a fivefold improvement in sensitivity. The entire methodology, while solely relying on commercially available reagents and instruments, could nonetheless achieve high labeling efficiency in the range of 50 to 100 Bq per cell. Last, the measured single-cell PET signal only arises from live cells, which bolsters the specificity of the assay. Collectively, these advances will facilitate widespread adoption of this technique while providing a reliable, straightforward, and accurate method for tracking multiple cells in vivo in crucial biological experiments.

[1]School of Medicine, Department of Radiation Oncology and Medical Physics, Stanford University, Stanford, CA 94305, USA. [2]School of Medicine, Department of Radiological Sciences, Stanford University, Stanford, CA 94305, USA. [3]School of Medicine, Department of Surgery, Stanford University, Stanford, CA 94305, USA. [4]Department of Biomedical Engineering, University of California, Davis, Davis, CA 95616, USA. [5]Department of Radiology, University of California, Davis, Davis, CA 95616, USA.
*Corresponding author. Email: pratx@stanford.edu
†Deceased.

RESULTS

A streamlined workflow for cell radiolabeling and dispensing

A crucial step toward the routine use of PET for tracking single cells in vivo is the design of an efficient and straightforward workflow for radiolabeling and dispensing single cells (Fig. 1). The key features of this method are that (i) labeling is achieved through a commonly available PET tracer, ^{18}F-fluorodeoxyglucose (FDG), and (ii) single cells are dispensed using an automated microfluidics device. Compared to other radiolabeling techniques, FDG can be inexpensively sourced from commercial vendors and central facilities without requiring specialized radiochemistry; hence, the method can be easily adopted by other researchers. Another advantage of FDG over ^{68}Ga-MSN lies in its longer half-life (2 hours) and shorter positron range, which translates into more accurate localization of single cells over longer periods of time. In addition, the use of an automated single-cell dispenser shortens the time required for isolating and dispensing viable single cells by eliminating the laborious steps involved in limiting cell dilution and microscopic verification. We further enhanced the detectability of single cells using a dual-layer bismuth germanium oxide/lutetium-yttrium oxyorthosilicate (BGO/LYSO) PET scanner (*15*, *16*), capable of high sensitivity (~10.4%) and resolution (~1.2 mm). Notably, the use of BGO as a scintillator material in this scanner results in a lower rate of background coincidence events compared to lutetium-based scintillators, which is a crucial advantage when imaging weakly radioactive cells. These background events are due to the natural occurrence of radioactive ^{176}Lu in the scintillator material (*17*, *18*).

As previously, we here focus on cancer metastasis as a model application for assessing the performance of PET for tracking the spread of single cells in vivo. B16 murine melanoma cancer cells were radiolabeled by incubating them with FDG (370 MBq/ml) for 1 hour after "fasting" for 1 hour in glucose-free media. After washing residual FDG, single FDG-labeled cells were dispensed into microcentrifuge tubes using a microfluidic-based cell sorter. This device achieves approximately 90% efficiency in dispensing the desired number of single cells (fig. S1). Consistent with our previous findings (*12*), these single cells appeared as distinct focal spots in PET images (Fig. 2A and fig. S2). To demonstrate that these focal spots were indicative of single cells, we partitioned the contents of each vial into two or three new vials and imaged the samples a second time (fig. S2A). We also used gamma counting to measure the radioactivity of the vial before and after partitioning the samples (fig. S3). In nearly all experiments, the radioactivity remained confined to a single vial after partitioning, indicating that the vials initially contained single cells, which could not be split among multiple vials. In rare cases (<5%), however, we observed radioactivity in two or more vials after partitioning, which we attributed to the presence of multiple cells in the sample or the release of the radioactivity into the medium following the death of a labeled cell. To further investigate the latter scenario, we used PET to image cells that were deliberately killed by adding lysis buffer. In these samples, the PET signal was not confined to a localized focal point but was instead distributed within the entire vial (Fig. 2B and fig. S2B). Thus, since FDG diffuses out of a cell upon its death, the presence of focal signals in PET images specifically reflects the integrity of the cell membrane and, by extension, the viability the cells. Collectively, these in vitro results demonstrate the benefits of combining FDG labeling with microfluidic cell dispensing to visualize multiple cells efficiently and reliably by PET imaging.

Labeling efficiency was further characterized by single-cell gamma counting for three cancer cell lines: murine melanoma B16, murine breast cancer 4T1, and human breast cancer MDA-MB-231 (Fig. 2C). These cell lines were selected owing to their ability to withstand exposure to ionizing radiation during radiolabeling (*19*, *20*). Mean FDG uptake was highest for B16 cells (52 Bq per cell), followed by MDA-MB-231 (32 Bq per cell) and 4T1 cells (13 Bq per cell). The observed difference in FDG uptake was likely due to intrinsic differences in basal glucose metabolism. Compared to the labeling method based on ^{68}Ga-MSNs reported by Jung *et al.* (*12*), where average activity for MDA-MB-231–labeled cells varied between 3 and 10 Bq per cell batch to batch, the labeling protocol using FDG was more consistent and yielded higher average activity within the same cell line. In addition, the radioactivity of single cells can be measured using PET by computing the average uptake within regions of interest (ROIs) centered on individual cells. The cell activity characterized through this method was consistent with the radioactivity measured using a gamma counter (fig. S4), thus suggesting that PET can quantitatively measure single-cell activity in vivo.

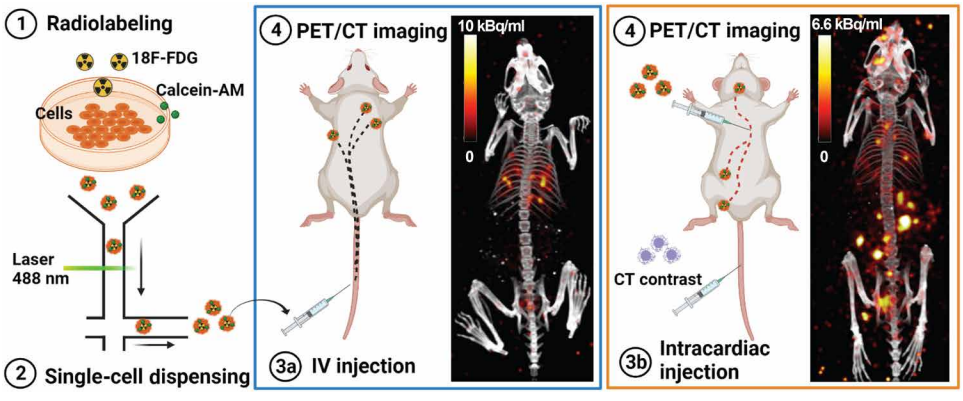

Fig. 1. Workflow for tracking single radiolabeled cells in vivo with PET. Cancer cells (B16) were radiolabeled with FDG (1) and then sorted and dispensed as single cells using a microfluidic device (2). As a proof of concept, the labeled cells were injected into a murine model via either intravenous (IV) (3a) or intracardiac (3b) routes. Cells injected intravenously were trapped in the lungs, whereas those injected intracardially were widely disseminated throughout the entire body. We used PET/CT and a custom algorithm to estimate the 3D locations of these single cells (4). Figure 1 was created in part with BioRender.com.

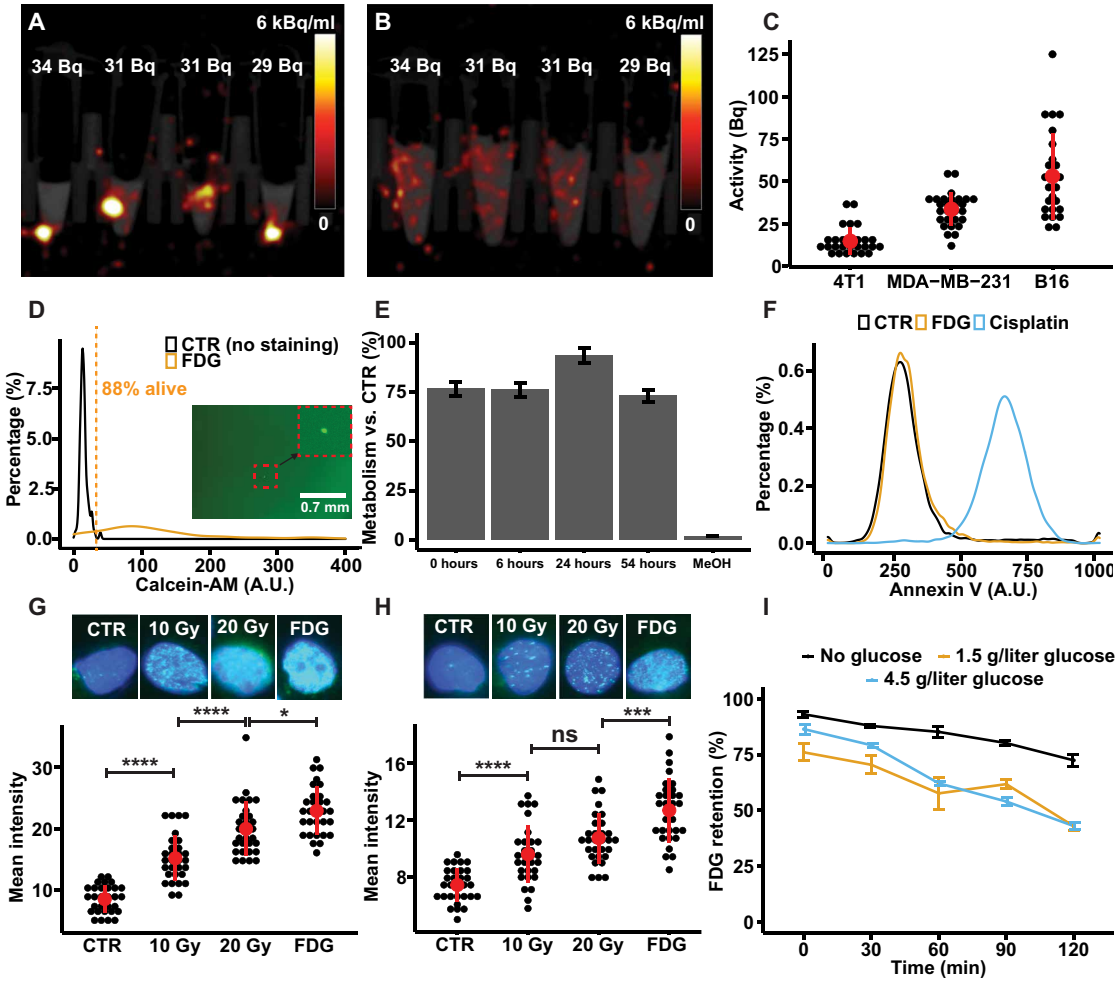

Fig. 2. In vitro characterization of FDG cell labeling. (**A** and **B**) Single FDG-labeled cells (B16) were placed in vials and imaged with PET/CT before and after adding lysis buffer, showing that focal PET signal is a characteristic feature of live cells. PET images are fused with CT and displayed as maximum intensity projections, with a slice thickness of 6 mm to capture the contents of the entire vial. (**C**) The radioactivity of single cells was measured with a gamma counter, revealing that B16 cells could be labeled with FDG more effectively than MDA-MB-231 and 4T1 cells. (**D**) Viability of FDG-labeled cells was >88%, as assessed by calcein-AM staining. Inset picture: Fluorescence micrograph confirming that dispensing of exactly one cell by the device. (**E**) CCK-8 assay, demonstrating a 75% cell metabolic rate 54 hours after labeling, relative to control cells (the number of biological replicates in each group is three). (**F**) Annexin V assay, showing comparable levels of cell apoptosis in labeled and control cells 3 hours after labeling and substantially less than the positive control (cisplatin). (**G** and **H**) DNA damage characterized using γH2AX staining for control, x-ray irradiated, and FDG-labeled cells, measured 10 min (G) and 24 hours after labeling (H). (**I**) FDG efflux from FDG-labeled cells in the presence of different concentrations of D-glucose (0, 1.5, and 4.5 g/liter) (the number of biological replicates in each group is three). CTR, control; A.U., arbitrary units; MeOH, methanol; ns, not significant.

We also found that FDG uptake was strongly influenced by the concentration of glucose in the media. Although we labeled cells in glucose-free media, a small amount of glucose was present in the fetal bovine serum (FBS) supplement, which ended up substantially influencing the efficiency of the labeling procedure (fig. S5). Relative to standard 10% FBS media [glucose (12.5 mg/dl)], FDG uptake increased significantly when using 1% FBS media [glucose (1.25 mg/dl)]. There was no significant difference when we further reduced glucose concentration using 10% dialyzed FBS [glucose (0.1 mg/dl)]. The presence of FBS was necessary for the viability and normal metabolism of cells, as we observed reduced uptake when FBS was withheld from the media. On the basis of these results, we selected 1% FBS as the standard condition for cell labeling.

In addition, we examined the effect of FDG labeling on the viability and behavior of B16 cells according to several assays. Exposure to ionizing radiation during the labeling procedure may interfere with the normal functions of the labeled cells. Calcein-acetoxymethyl (calcein-AM) was used as a marker of cell viability during single-cell dispensing. Analysis of FDG-labeled cells revealed that 88% of them were positive for calcein-AM staining (gated above the autofluorescence signal of the control cells; Fig. 2D). To further assess the potential toxicity of the labeling procedure, metabolic activity was measured at times 0, 6, 24, and 54 hours using the colony-counting kit colorimetric assay [Cell Counting Kit 8 (CCK-8)]. Compared to control cells, FDG-labeled cells maintained >75% metabolism for up to 54 hours postlabeling (Fig. 2E).

We further investigated the biological fate of labeled cells and whether they underwent apoptotic or necrotic cell death following exposure to radioactivity, using annexin V and Sytox Green as markers for these events. Three hours after FDG labeling, no substantial

increase in annexin V staining was observed relative to control cells. In contrast, cells treated with cisplatin (positive control; 100 μM, 48 hours) demonstrated strong binding of the marker (Fig. 2F). FDG-labeled cells also presented minimal Sytox signal, indicating that the cell membrane remained intact following radiolabeling (fig. S6), although moderate lipid peroxidation (~20%) could be detected, which was higher than that of x-ray irradiated samples (~5%) but substantially lower than the positive control (~99%; fig. S7).

DNA damage commonly occurs following radiation exposure. To quantify this effect, we measured DNA double-strand break by γH2AX immunostaining. As a reference, the intensity of the γH2AX signal was also measured for cells exposed to 10 and 20 Gy of x-ray radiation (Fig. 2G). Together, these results suggest considerable DNA damage 10 min postradiation, although the damage was substantially repaired 24 hours after radiolabeling (Fig. 2H). In our estimate, most of the DNA damage is incurred during the hour-long incubation with FDG. A calculation based on a dose point kernel (*21*) suggests that the absorbed dose experienced by the cells during the 1-hour incubation was approximately 33 Gy (Supplementary Methods and fig. S8). Because positrons deposit their energy over a distance much longer (~1 mm) than the typical cell diameter (0.01 mm), the radiation dose experienced by the labeled cells in vivo is only a small fraction (<1%) of the total emitted radiation.

To further characterize the behavior of FDG-labeled cells, we assessed the migration of B16 cells in vitro in response to a small mechanical scratch to the surface of the cell monolayer. On the basis of observations at 0, 6, 24, and 48 hours, we found that FDG-labeled cells could close the gap at a rate similar to control cells, whereas the gap expanded for cells treated with cisplatin (positive control; 100 μM for 48 hours) during the observation period (fig. S9). To further characterize the metastatic potential of FDG-labeled cells, we performed a Transwell migration assay, an in vitro technique that evaluates the ability of cells to migrate through a membrane toward a chemoattractant. The findings from this assay demonstrated that the motility of FDG-labeled cells is similar to that of unlabeled cells (fig. S10), thus suggesting that the labeling procedure did not affect the ability of the cells to migrate in vitro.

Last, we studied the rate of FDG efflux from labeled B16 cells for media containing different glucose concentrations [D-glucose (0, 1.5, and 4.5 g/liter)]. Cellular efflux of the radiotracer can lower tracking accuracy by causing loss of cell signal and higher background radioactivity. At the 120-min time point, cells retained upward of 75% of the initial FDG radioactivity in glucose-free media, compared to 48% when higher glucose concentrations (1.5 and 4.5 g/liter) were present (Fig. 2I). The influence of extracellular glucose on FDG efflux from the labeled cells is relevant considering the typical concentration of glucose in the blood of healthy fasting mice (0.8 to 1 g/liter) (*22*). In addition, FDG metabolites were not detected in the extracellular environment, suggesting that the efflux of the radiotracer predominantly occurs in the form of unphosphorylated FDG (fig. S11).

In summary, high labeling radioactivity could be achieved with FDG, and most labeled cells remained viable throughout the time frame of a typical ^{18}F tracking experiment (a few hours). While an increase in DNA damage was noted, the labeling procedure did not alter the ability of tumor cells to migrate in vitro. Efflux was increased in the presence of extracellular glucose, yet cells retained approximately half of the initial labeling radioactivity, which is comparable to other labeling strategies.

In vivo imaging of multiple FDG-labeled individual cells with PET

Having characterized the in vitro efficacy and potential toxicity of FDG as a labeling agent, we then examined its in vivo tracking performance. Approximately 20 radiolabeled B16 cells were introduced into female nude mice (*Foxn1^{nu}*) via intravenous or intracardiac injection (Fig. 3). Following injection, mice were imaged using PET (10-min acquisition), and images were reconstructed using the conventional ordered subset expectation maximization (OSEM) algorithm provided by the vendor (Sofie Biosciences). After adjusting the display window, we were able to visualize punctate signals originating from various organs within the mice. Consistent with our previous study (*12*), these signals appeared as discrete focal spots (green arrows; Fig. 3, A and C), closely resembling the imaging pattern observed when imaging in vitro samples. The signals were confined to the body of the mice and were clearly distinct from high-frequency reconstruction noise (blue arrows), which can be observed near the edge of the field of view. Typically, reconstruction noise is confined to one to two adjacent pixels, whereas the signals observed in these PET images are Gaussian in shape and spread over a larger number of pixels. In addition, cell signals appear at consistent locations across multiple frames, whereas reconstruction noise is stochastic. In view of these factors, we conclude that the observed PET signals represent FDG-labeled cells.

Extensive ex vivo analyses were conducted to confirm that focal PET signals reflect the presence of arrested single cancer cells. First, FDG-labeled B16 cells were injected into the left ventricle of a *Fox1^{nu}* mouse, and their arrest location was mapped to specific organs based on coregistered PET and computed tomography (CT) information. The lungs and surrounding organs were then excised and imaged again, using the same protocol. Despite challenges in ensuring that single cells are not flushed out during the dissection process, ex vivo gamma counting and PET imaging of the excised organs are consistent with in vivo PET imaging findings (fig. S12). As further corroboration, a single B16 cell, labeled with both FDG and the fluorescent dye DiO, was intravenously injected into a BalB/C mouse and tracked to the lungs. The mouse's organs were excised and imaged again, allowing us to precisely pinpoint the location of the cell within the excised lungs. Using this information, we extracted a small sample of lung tissue (~2-mm thick) and confirmed by gamma counting the presence within it of detectable radioactivity (19 Bq). Last, the lung tissue samples were made optically clear, and the presence of a single cancer cell was confirmed by fluorescence imaging of the same tissue (fig. S13).

As would be expected, markedly different patterns of cellular arrest arose from different injection routes. After intravenous injection (Fig. 3A), the administered cells were confined to the lungs, which is the first capillary network on their path, whereas after intracardiac injection (Fig. 3C), the cells appeared to spread across multiple organs. It is important to note that about 10 to 20 cells could be simultaneously visualized within each animal, supporting the feasibility of tracking multiple single cells in vivo using PET.

Previously, Jung *et al.* (*12*) reported intravenous injection of 100 cells labeled with ^{68}Ga-MSNs. However, in their study, it was difficult to distinguish individual labeled cells from background signal, partly because of the low activity of the cells (average ~3 Bq per cell). In our study, we could consistently label B16 cells with >20 Bq. These FDG-labeled cells were remarkably robust, producing a stable signal for up to 100 min postinjection. In addition, the PET images

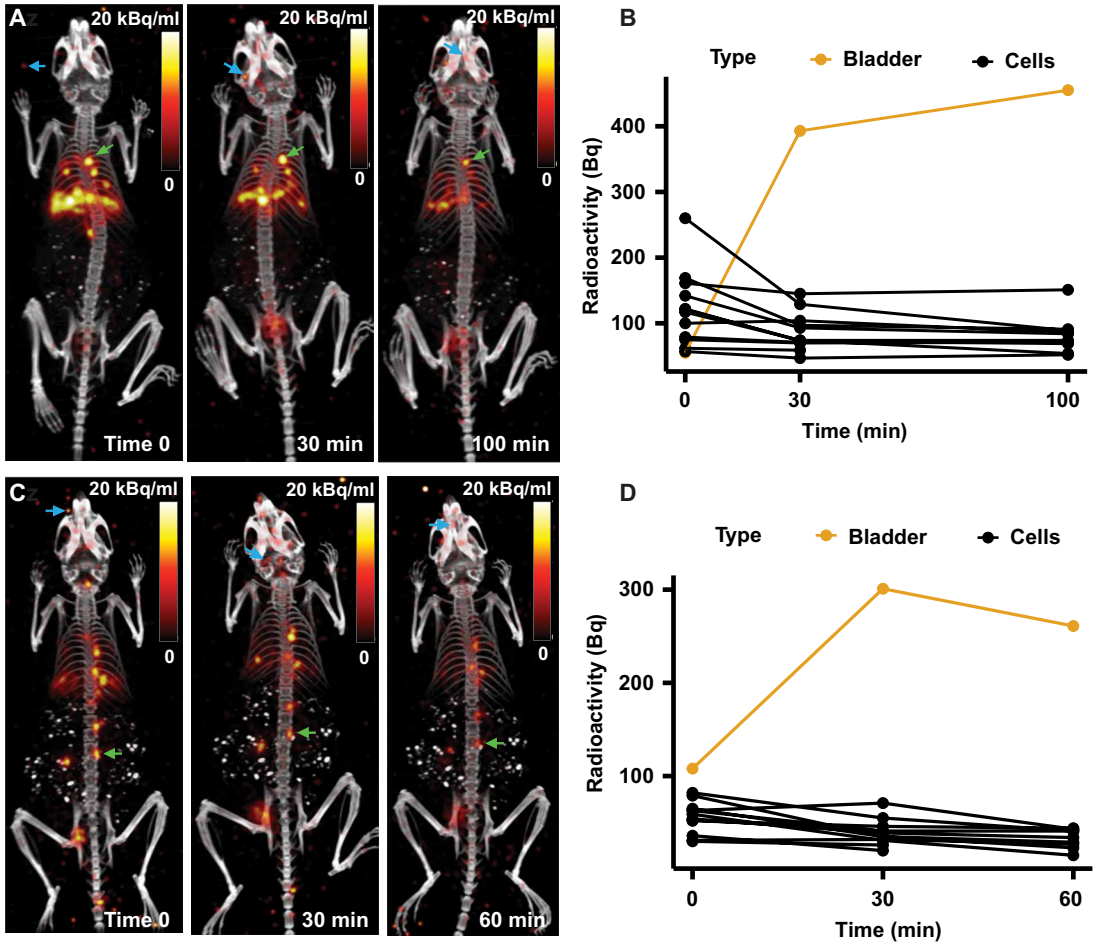

Fig. 3. In vivo PET imaging of FDG-labeled single cells. (**A** and **C**) PET/CT images of radiolabeled single cells, which were introduced into mice via intravenous (A) or intracardiac injection (C). PET images were reconstructed using the conventional OSEM method. The focal signals seen in the PET images represent single labeled cells (green arrows). High-frequency reconstruction noise is also visible in the images near the edge of the field of view (blue arrows). (**B** and **D**) ROI quantification of the PET images, showing the change in radioactivity in single cells and bladder over time. PET and CT images are fused together and displayed as maximum intensity projections, with a slice thickness of 21.2 mm.

had a minimal background in the mouse body, apart from a small amount of FDG visible in the mouse bladder (Fig. 3, A and C).

To characterize the dynamic evolution of the labeled cells, we monitored the radioactivity of single cells by quantifying their radioactivity within ROIs at different time points (Fig. 3, B and D). Immediately after intravenous and intracardiac injections, the mean radioactivity per cell was 122 and 56 Bq, respectively. These numbers rapidly dropped to 86 and 38 Bq after 30 min but then seemed to stabilize at around 82 and 33 Bq per cell at later time points. This decrease was accompanied by increasing PET signal in the bladder, where activity from cell efflux accumulated over time. From these data, we conclude that conventional OSEM reconstruction can monitor the migration of single cells to various sites throughout the body, using PET data from a 10-min scan.

Enhanced detection of single cells using the PEPT-EM algorithm

While our results show that OSEM can be used to visualize single cells in vivo, we aimed to further improve the sensitivity of PET for this demanding application by investigating the performance of an algorithm recently developed for tracking multiple moving particles in industrial processes and other opaque systems. Positron emission particle tracking (PEPT) is a method developed on the premise that conventional PET is not optimal for localizing a small number of weakly radioactive point sources (*23*–*25*). PET requires data to be reconstructed into a large tomographic image composed of millions of voxels, which does not efficiently represent point sources. In contrast, PEPT calculates the three-dimensional (3D) positions of the sources directly from the coincident annihilation photons recorded by the scanner without explicitly reconstructing an image of the radiotracer distribution. Recently, an expectation-maximization formulation (PEPT-EM) was derived to reconstruct source locations based on a maximum-likelihood approach and could track up to 80 moving simulated particles simultaneously (*26*). However, the method has yet to be investigated for tracking cells in vivo.

The difference between PEPT-EM and conventional OSEM is illustrated in Fig. 4 (A and C). Both algorithms are iterative, starting with an initial estimate of the image or source positions, followed by several iterations to update the initial guess according to the measured PET data. In the case of OSEM, the input data are binned into

sinograms, and the outputs are tomographic PET images. OSEM alternates forward- and back-projections to maximize the agreement between the estimated and measured sinograms. PEPT-EM, on the other hand, operates directly on the raw list-mode data, first soft-clustering the recorded coincidence events according to their proximity to discrete radioactive sources and then updating the 3D positions of these sources based on a distance minimization procedure. Theoretically, two nearly intersecting lines of response (LORs) are sufficient to determine the location of a radioactive source. However, in practice, many more LORs are required to cope with various sources of uncertainty, including intrinsic background radioactivity and photon scatter.

To evaluate the performance of the PEPT-EM algorithm for tracking single cells, we labeled five B16 cells with FDG, dispensed them in individual vials, and then imaged them using PET (Fig. 4, B and D). Using conventional OSEM reconstruction, we observed focal PET signals for cells containing as little as 12 Bq but could not resolve weaker cells. In comparison, PEPT-EM could correctly localize all five cells, including one containing only 4 Bq. Hence, PEPT-EM is more sensitive than OSEM for localizing weak point sources such as radiolabeled single cells.

To illustrate the convergence of the algorithm toward its solution, we plotted the estimated positions of these five cells after 0, 3, and 20 iterations (Fig. 4E and movie S1). Here, the center of each circle represents the estimated position of each cell, whereas the radius represents the SD of the estimate. The PEPT-EM algorithm was initialized with random cell locations. As the algorithm iterated, it clustered the list-mode data according to the likelihood that each detected event originated from each of the different cells being tracked. As the algorithm converged toward the maximum-likelihood location of the cells, the SD decreased from an initial value of 5 mm down to ~1.0 ± 0.1 mm. The most radioactive cell (32 Bq) converged the fastest and took only 3 iterations to settle, whereas the weakest cell (4 Bq) converged last, after 20 iterations.

We next used PEPT-EM to track the dissemination of melanoma cells in vivo. Around 20 FDG-labeled B16 cells were injected into nude mice (*Foxn1*^{nu}) via intravenous or intracardiac routes, and then PET/CT scans of these mice were acquired in list-mode format. The PET data were first reconstructed using the OSEM method to produce conventional tomographic images showing the distribution of the tracer in 3D. As previously shown, after intravenous injection, melanoma cells could be clearly seen in the lungs (Fig. 5A and movie S2), whereas after intracardiac injection, they were widely disseminated throughout the entire body and could be observed in many different organs (Fig. 5B and movie S3). We then reconstructed the list-mode data using PEPT-EM to derive the precise 3D single-cell locations for both injection routes.

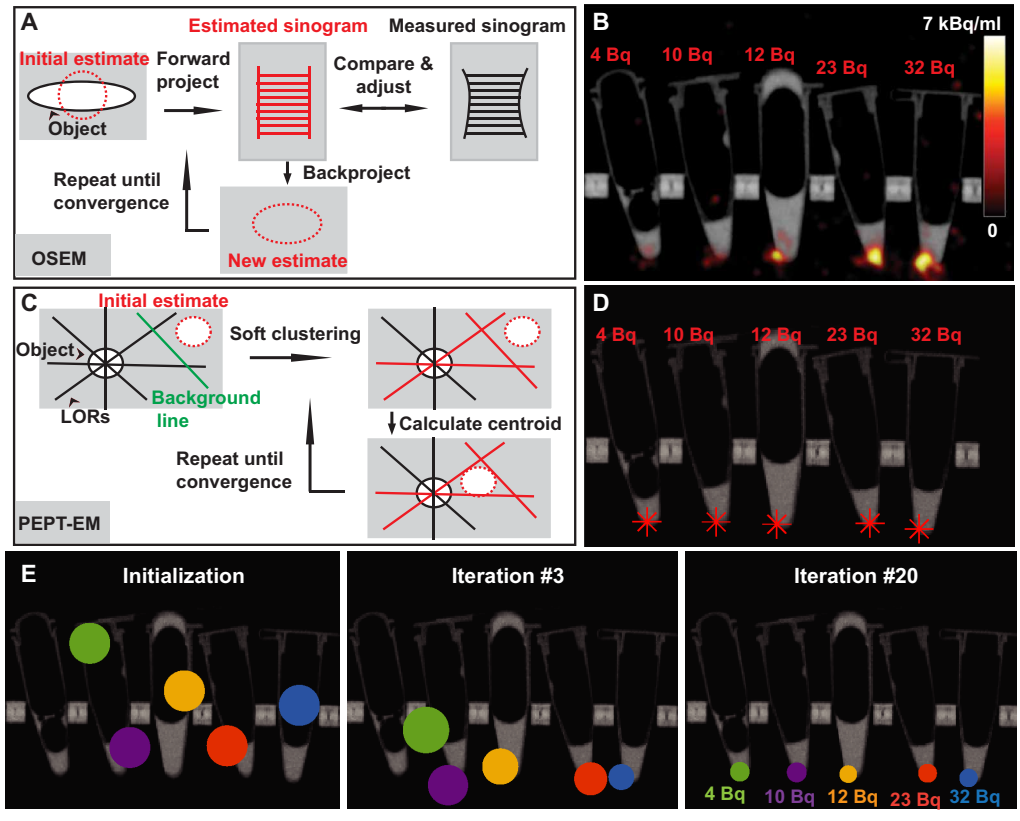

Fig. 4. PEPT-EM improves the detection of single cells. (**A**) Schematic representation of OSEM, the standard algorithm for PET reconstruction. (**B**) PET image obtained by OSEM reconstruction, showing five FDG-labeled cells imaged in vials. The lowest detectable cell had 12 Bq. PET images are displayed as maximum intensity projections, with a slice thickness of 7.1 mm, and fused to CT. (**C**) Schematic representation of PEPT-EM, a tracking algorithm based on a Gaussian mixture model that estimates the 3D positions of radioactive sources directly from the recorded coincident annihilation photons. (**D**) The 3D positions of the discrete sources were reconstructed by PEPT-EM from the same PET dataset, shown here as red asterisks over the CT image of the vials. (**E**) The PEPT-EM algorithm was initialized by generating random cell locations. As the algorithm iterates, it progressively converges toward the maximum-likelihood location of the cells, leading to a reduction in the SD of the estimated position (represented by the radius of the circle).

Overall, the cell locations estimated by PEPT-EM matched the positions where focal signals were observed in the OSEM-reconstructed PET image (Fig. 5, A and B). Because of physiological FDG accumulation in the bladder, PEPT-EM automatically assigns one of the sources to this organ. Unlike OSEM, PEPT-EM directly provides an estimate of the number of sources in the field of view and their 3D position. As the number of injected cells is not exactly known, we initialized PEPT-EM assuming a large number of cells (90 clusters) and filtered out any reconstructed cluster that did not meet specific requirements in terms of minimum radioactivity and variance. In general, the PEPT-EM algorithm does not converge to a single global solution. However, by initializing the algorithm using more sources than physically present, we can better sample the solution space and improve the convergence of the algorithm toward the global solution. Here, the initial source positions were randomly generated near the center of the mouse. To confirm that the outcome of the algorithm is independent of its initialization, we reconstructed the intracardiac dataset four times using different random initial positions and confirmed that the same solution is achieved independently of the initialization (fig. S14). Moreover, the same solution was obtained regardless of whether the sources were initially positioned near the center of the mice or randomized over the entire body. Movie S4 illustrates the convergence of the algorithm over 300 iterations.

In addition, we analyzed the performance of PEPT-EM under low-count conditions, which we simulated by splitting the 10-min PET acquisition into 10 frames of 1 min. When applied to the smaller datasets, PEPT-EM yielded 3D cell positions that were consistent with the full 10-min dataset. The computed positions appeared to fluctuate slightly from frame to frame, but the variations were within the spatial resolution of the system and likely caused by statistical noise rather than physiological cell motion (Fig. 5C, bottom). In contrast, because of the low statistics, OSEM reconstruction of the 1-min acquisition was noisy and failed to resolve single cells (Fig. 5C, top). This result confirms our previous observation that PEPT-EM is more sensitive for tracking weakly radioactive single cells.

Last, we conducted Monte Carlo simulations of low-radioactivity sources to complement our experimental findings. The geometry and physical characteristics of the GNEXT PET scanner were modeled using the GATE software (Supplementary Methods). At the center of the field of view, a water phantom (4 cm in diameter and 8 cm in length) was placed that contained a variable number of randomly positioned ^{18}F sources. List-mode PET data were simulated and reconstructed using PEPT-EM. Using the ground-truth source locations as our reference, we found that PEPT-EM could localize as many as 20 sources with accuracy below 1 mm (fig. S15). A minimum radioactivity of 5 Bq per source and source-source separation of 5 mm were sufficient to enable reliable tracking performance (success rate of more than 90%; fig. S16). These results are aligned with experimental findings and underscore the potential of PEPT-EM for localizing multiple weak sources in vivo.

Fate of radiolabeled single cells following intracardiac injection

Intracardiac injection is commonly used as an experimental mouse model of bone metastasis (*27*–*29*). However, the procedure is technically challenging, and a high degree of precision is required to inject the cells into the small and pulsing volume of the left cardiac ventricle (movie S5). Even with ultrasound guidance, it can be difficult to confirm whether an injection was performed correctly. Using our imaging technique, we observed three different scenarios following intracardiac injection: (i) The cells were correctly injected into the left ventricle of the mouse and distributed throughout the entire body; (ii) the cells were inadvertently injected into the nearby right ventricle and trafficked to the lungs, where they arrested; and (iii) the cells were injected outside of the heart into the pericardial cavity (fig. S17). In this context, the ability of PET to track the fate of

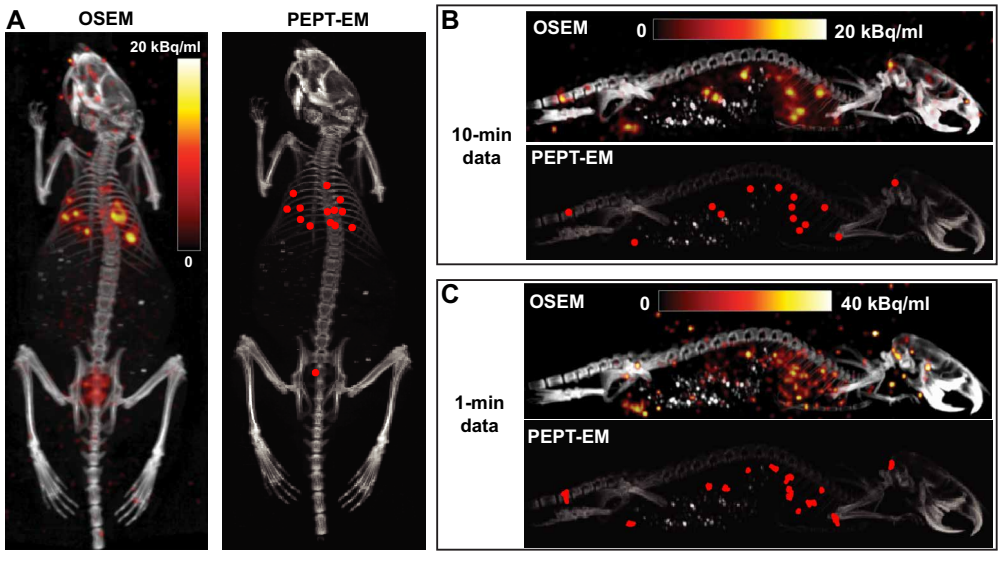

Fig. 5. In vivo tracking single cells using PEPT-EM. (**A**) The PEPT-EM algorithm was applied to a PET dataset acquired after intravenously injecting 10 to 20 single cells into *Foxn1*^{nu} mice. The resulting cell positions (red asterisks; right) are compared to the conventional OSEM reconstruction of the same dataset (left). (**B** and **C**) Both algorithms were also applied to a PET dataset obtained by injecting FDG-labeled cells into the left ventricle of a mouse. The results are shown for 10-min (B) and 1-min acquisitions (C). Fused PET/CT images are shown as maximum intensity projections, with a slice thickness of 21.2 mm (coronal view) and 20.2 mm (sagittal view).

single cells could help establish more reliable models of bone metastasis by confirming the successful administration of cells.

To further illustrate the unique capabilities of the proposed cell tracking methodology, we traced the fate of 74 FDG-labeled melanoma cells after intracardiac injection in healthy *Foxn1*^{nu} mice ($n = 6$). We evaluated the spatial distribution of the arrested cells using coregistered CT images to identify the anatomical sites where single cancer cells were seen to arrest (Fig. 6A and figs. S18 and S19). These sites were then systematically categorized according to conventional organ systems, distinguished by color-coded groupings (Fig. 6B). We observed that a substantial number of cells arrested in large organ systems, such as lung, musculoskeletal, and digestive systems. This pattern of cellular arrest was qualitatively reproduced in an immunocompetent model system (C57BL/6 mice; $n = 3$; fig. S20). The results are consistent with the formation of bone metastases that are known to arise in this animal model (*29*–*31*).

Last, we examined the pattern of cell arrest in relation to the vascular system, which was imaged using a nanoparticle-based CT contrast agent. The agent, which was introduced intravenously in mice after intracardiac injection of cancer cells, remained detectable in the bloodstream for 30 min, with a peak observed at around 15 min (fig. S21). Because of the 100-μm resolution of this scan, we could clearly resolve larger arteries such as the aorta, carotid arteries, and jugular veins but not smaller tissue capillaries. However, the location of the arrested cells seen on PET did not correlate with the larger vessels visible on CT. This observation suggests that the labeled cancer cells were likely trapped in the smaller capillaries within the tissues (Fig 6C and movie S6).

DISCUSSION

Collectively, our results show that PET is sensitive enough to track the individual fate of 10 or more cells simultaneously in the same animal. This study represents an important improvement over our previous work (*12*), where we could only track cells one at a time (Table 1). The improved tracking workflow solves a crucial bottleneck by enabling multiple cells to be tracked simultaneously, markedly increasing the amount of information that can be garnered through each experiment. This crucial benefit is vividly illustrated in our analysis, which tracked the fate of 74 single cells in six mice (Fig. 6). If performed using our prior single-cell method and considering the success rate for intracardiac injection, such a study would have required preparing and imaging well over 100 mice, which would have been prohibitive.

In addition, the workflow reported herein solely relies on commercially available reagents and instruments. Contrary to expectations, metabolically active cancer cells (e.g., B16) could be reliably labeled with 25 to 100 Bq of FDG per single cell, an amount largely sufficient for high-accuracy tracking (Fig. 2C). The labeling protocol is straightforward and involves only short-term withdrawal of glucose from the media, without any nanoparticle radiochemistry. In addition, ^{18}F is advantageous from the perspective of imaging physics as it has a shorter positron range (1 mm) than ^{68}Ga (2.9 mm), which improves tracking accuracy (*32*). This workflow also benefited from the use of a high-sensitivity, high-resolution, low-background, dual-layer (BGO/LYSO) preclinical PET scanner to image the labeled cells (*15*, *16*), which considerably improved the detectability of weakly labeled cells. Last, we used a microfluidic device to select and dispense fixed numbers of FDG-labeled cells, which improved reliability and reduced the preparation time to less than 10 min.

While being more straightforward, FDG labeling demonstrated performance comparable to nanoparticle-based labeling. FDG-labeled cells appeared as tiny hot spots, closely resembling the previously observed pattern of cells labeled with ^{68}Ga-MSNs. These cells maintained high metabolic activity (>75% for up to 54 hours; Fig. 2E), a figure, however, slightly lower than for cells labeled with ^{68}Ga (90% for up to 50 hours). This lower metabolism after FDG labeling is likely caused by DNA damage, which was equivalent to an x-ray dose of more than 20 Gy (Fig. 2, G and H). DNA damage is known to cause transient cell cycle arrest, which could explain the observed decrease in metabolism. However, given the short half-life of ^{18}F, tracking experiments are limited to a short time frame of a few hours, during which the effects of radiation exposure have not yet manifested themselves (Fig. 2, D and F, and fig. S6). In the rare instance

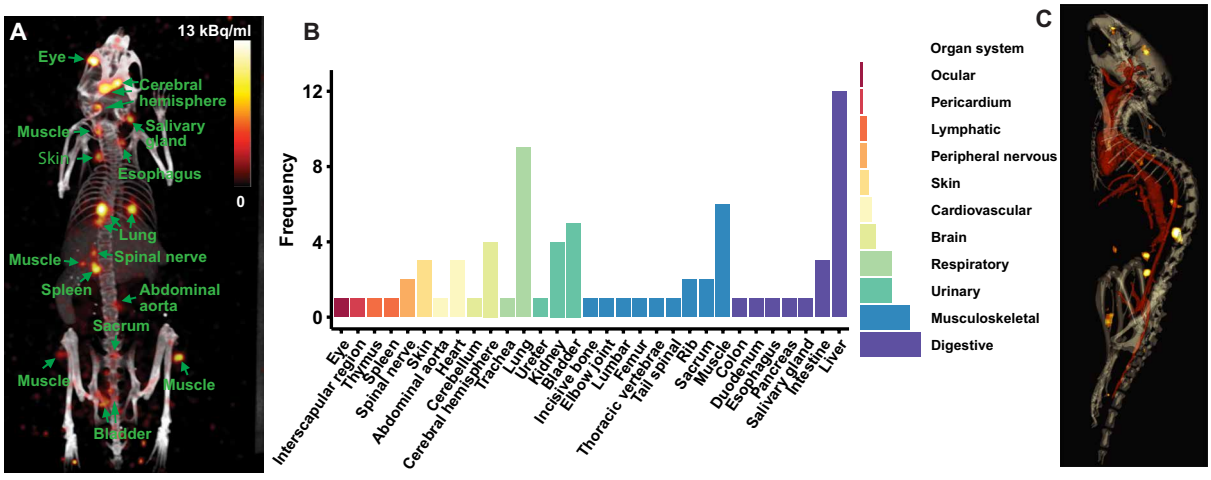

Fig. 6. In vivo tracking of the fate of single cells after intracardiac injection. (**A**) PET/CT image (OSEM reconstruction; maximum intensity projection) of a mouse right after intracardiac (left ventricle) injection, with labels indicating the anatomical locations where cancer cells were arrested. Fused PET/CT images are displayed as maximum intensity projections, with a slice thickness of 21.2 mm. (**B**) A comprehensive summary of the results, showing the sites and organ systems in which 74 labeled cells arrested ($n = 6$ mice). (**C**) 3D rendering showing single-cell distribution (OSEM reconstruction) relative to the segmented bony and cardiovascular anatomy.

Table 1. Major advances reported in this study.

	Jung *et al.* (*12*)	This study	Rationale/outcome
Reconstruction method	CellGPS	PEPT-EM	PEPT-EM can track 20 cells in the same subject through multiplexing and improved sensitivity (4 Bq per cell).
Isotope	^{68}Ga	^{18}F	Shorter positron range and longer half-life of ^{18}F improves tracking accuracy.
Labeling agent	MSNs	FDG	FDG is approved for human use and achieves high cell labeling efficiency (>50 Bq per cell).
PET detectors	LSO	LYSO/BGO	LYSO/BGO detectors increase sensitivity and lower intrinsic background.
Single-cell isolation	Limiting dilution	Microfluidic cell dispenser	Automated dispensing improves reliability and shortens overall preparation time.
Cell injection	Intravenous	Intracardiac	Cells injected intracardially traffic to all major organs and provide a better model of metastatic spread.

that a cell does not survive, the ensuing release of FDG from its cytosol would cause its PET signal to vanish from the image (Fig. 2B), thus preventing dead cells from being included into further downstream analysis.

Another important finding is that PET could detect single cells labeled with as little as 4 Bq. This unprecedented level of sensitivity was achieved using a high-performance PET scanner for data acquisition and leveraging the strength of the PEPT-EM algorithm for cell detection. Using conventional OSEM, we achieved a limit of detection for single cells of 12 Bq using a dual-layer BGO/LYSO microPET scanner with 10.4% sensitivity (*15*, *16*), which compares favorably to the limit of 28 Bq previously achieved using a single-layer lutetium oxyorthosilicate (LSO) PET scanner (*12*). The detection limit was further lowered by reconstructing the data using the PEPT-EM algorithm, which, unlike OSEM, accounts for the discrete nature of the radioactive sources being tracked, thus turning an image reconstruction problem into a source localization problem. In turn, the improved detection limit of PEPT-EM translates into higher sensitivity for tracking single cells in vivo, which was particularly evident for low-count data (Fig. 5, B and C). Further lowering the limit of detection would extend the applicability of this technique to a broader range of applications, including tracking radiosensitive cells using low radioactivity or over long periods of time.

Despite the limitations associated with the use of radiation to label cells, the reported PET-based workflow is unique in enabling single cells to be tracked across the whole body. Only few methods can image the behaviors of single cells in vivo. One early technique relied on intravital microscopy to observe cell trafficking in vivo but faced limitations in penetration depth and field of view (*33*, *34*). Another optical method, bioluminescence imaging, can detect single cells using an efficient luciferase reporter, albeit with limited resolution and penetration depth (*35*). Magnetic resonance imaging is another feasible option but only for organs presenting a uniform background, such as the brain and liver, and with low temporal resolution (*36*, *37*). A related technique, magnetic particle imaging, offers high contrast and sensitivity, but achieving single-cell sensitivity remains aspirational given the limited loading capacity of cells for superparamagnetic iron oxide nanoparticles (*38*).

While this study focused primarily on imaging static cells, being able to image cells as they move would provide crucial insight into the dynamics of cell trafficking. Our results show that PEPT-EM could simultaneously track up to 14 single cells (mean radioactivity of 56 Bq per cell) with a temporal resolution of 1 min (Fig. 5C). PEPT-EM treats dynamic data as a series of independent frames, which limits its ability to track the motion of low-activity sources. In their initial demonstration, Manger *et al.* (*26*) used PEPT-EM to track the rotation of 10 ion-exchange resin particles labeled with 1- to 10-MBq radioactivity at velocities of up to 50 cm/s. Previously, our group developed a custom algorithm, CellGPS, for tracking the dynamics of a single cell in vivo (*12*, *13*). Using the CellGPS algorithm, we tracked the motion of a single cell (70 Bq) traveling at a maximum velocity of 5 cm/s, from its injection site in the tail vein to its ultimate arrest within pulmonary capillaries. Unlike PEPT-EM, the CellGPS algorithm models the trajectory of a moving cell as a continuous function of time and can thus reconstruct complex spatiotemporal trajectories from fewer detected counts. However, CellGPS is unable to track more than one cell at a time. We are now investigating the feasibility of combining PEPT-EM and CellGPS into a single algorithm to improve the temporal resolution for multiplexed cell tracking.

Additionally, this study explicitly examined the distribution of individual cancer cells throughout the entire body after intracardiac injection. Through this improved method, we could localize disseminated melanoma cells throughout the body with excellent spatial resolution. From coregistered CT images, we identified the organs where migrating cells tended to arrest and found that B16 cells were widely distributed throughout the mice, reaching 31 organs and 11 organ systems. This finding was expected given that the left cardiac ventricle supplies arterial blood to the entire body. Our data further suggest that cells arrested very quickly after injection,

within the first minute, likely through passive trapping in capillary beds. Prior studies of metastases formation following intracardiac injection mainly reported bone metastases (*27*, *30*, *31*), although the musculoskeletal system accounted for only 22% of the cell arrest in our study. This observation suggests that the bone marrow may provide a more supportive niche for the survival and rapid growth of metastatic lesions, as originally postulated in the "seed and soil" hypothesis (*39*, *40*).

While several advantages of FDG-PET for tracking single cells have been described, a few limitations should also be mentioned. The short half-life of ^{18}F of 110 min limits the tracking time frame to a few hours and hence prevents FDG from being used for tracking cells over multiple days, precluding tracking the migration of hematopoietic stem cells during bone marrow transplant or immune cell homing in response to inflammatory stimuli (*4*, *41*). FDG is better suited for short-term tracking applications, as reported in this study. For long-term tracking of radiolabeled cells, long-lived isotopes such as ^{89}Zr (3.3 days half-life) are available to track cells over 7 days (*12*). FDG may also be less efficient as a label for cells with low basal glucose metabolism, such as quiescent immune cells and stem cells. A suitable radiolabel should be selected considering the characteristics of the cells being tracked. Another limitation of FDG labeling is that cells suffered DNA damage from exposure to radiation during the 1-hour incubation with the radiotracer (370 MBq/ml). An alternative labeling method using a microfluidic device could label cells instantly, which would reduce DNA damage by avoiding prolonged radiation exposure during the labeling process (*42*–*44*).

MATERIALS AND METHODS

Cell culture

Two murine cancer cell lines (B16-F10 and 4T1) and one human cancer cell line (MDA-MB-231) were originally acquired from American Type Culture Collection (ATCC). We cultured B16-F10 and MDA-MB-231 in Dulbecco's modified Eagle's medium (DMEM) medium (Thermo Fisher Scientific, #11995065) and 4T1 cells in RPMI 1640 medium (ATCC, #302001). Unless otherwise noted, both cultured media were supplemented with 10% FBS (Thermo Fisher Scientific, #26140079) and 1% penicillin-streptomycin (Thermo Fisher Scientific, #15140122). The cells were cultivated in T25 culture flasks inside a humidified incubator at 37°C and 5% CO_2 until confluence and transferred to tissue culture plates for radiolabeling and biological assays. Cells used for radiolabeling and biological assays did not exceed passage 15.

Radiolabeling with FDG

B16-F10, 4T1, and MDA-MB-231 were first seeded into a six-well plate at 2×10^5 cells per well and were cultured for 48 hours. To enhance FDG uptake, these cells were kept for 1 hour in a glucose-free medium (DMEM medium with L-glutamine; Thermo Fisher Scientific, #11966025) and 1% FBS before radiolabeling. After this fasting period, we replaced the fasting media with fresh fasting media mixed with FDG (370 MBq/ml, 2 ml per well). Clinical-grade FDG was produced at the Stanford Cyclotron and Radiochemistry Facility through nucleophilic ^{18}F-fluorination and hydrolysis of mannose triflate. The radiotracer was picked up within 2 hours of production to ensure high specific activity. We incubated cells with FDG for 1 hour and then washed each well three times with 2 ml of phosphate-buffered saline (PBS) to remove residual extracellular FDG.

Single-cell dispensing

We used a microfluidic-based single-cell sorter (Hana, Namocell) to dispense single cells into a 96-well plate. We first stained the cells with calcein-AM (5 nM; Thermo Fisher Scientific, #65085381; 8-min incubation) and diluted the cell suspension to achieve 5000 to 10,000 cells/ml. As per the device's instruction for dispensing single cells, we loaded the diluted cell solution into a cell cartridge and ran the device in analysis mode to differentiate live cells from dead cells and debris. After analyzing around 200 cells, we gated out the debris population (defined by low forward scattering and side scattering values) and selected viable cells with strong green fluorescence (typically, the threshold was set at 50). We then ran the device in dispensing mode to dispense 30 single cells into the media-prefilled wells of a 96-well plate. Each single cell was dispensed inside a 1-μl droplet by the device.

Single-cell gamma counting

An automatic gamma counter system (Hidex) was used to measure the radioactivity of individual cells. Single radiolabeled cells were transferred to 250-μl microcentrifuge tubes and loaded into racks for automated gamma counting. Each tube contained 100 μl of fresh media and a 1-μl droplet from the single-cell dispenser (composed of 99.7% PBS sheath fluid, 0.3% cell culture media solution). As a result, the radioactivity in each tube mainly originated from the single cell as the efflux in the cell solution was highly diluted. The radioactivity values in counts per second were converted to Bq through a calibration curve constructed from the measurement of serially diluted FDG solutions and a standard dose calibrator (Biodex, Atomlab 400). To confirm the singularity of dispensed single cells, we divided the solution in each tube equally into two or three vials and measured the activity of each fraction by gamma counting and PET imaging. The rationale for this experiment is that the contents of the single cell cannot be fractionated into multiple vials.

Microscopic verification of single cells

Fluorescence microscopy was used to confirm the number of single cells dispensed by the single-cell sorter. A B16 cell suspension was prepared at a density of 10^6 cells/ml in serum-free DMEM culture media. DiO dye (Invitrogen, #V22886) was added at a concentration of 5 μM, followed by a 10-min incubation at 37°C. After washing once with PBS, various numbers of single cells (1, 5, 10, 20, and 40) were dispensed into the wells of a 96-well plate using a single-cell sorter device (Namocell, Hana). After dispensing, the cells were incubated in complete media in the cell culture incubator for 2 hours to allow them to settle to the bottom of the well. We then used a fluorescent microscope with a motorized stage (Leica, DMi8) to scan each well and image the single cells. The number of cells dispensed was manually counted for each group (six samples per group).

Cell viability assays

The effect of radiolabeling on cell metabolism was assessed using the colorimetric CCK-8 assay. B16 cells were first seeded onto a 96-well plate at a cell density of 5000 cells per well and grown for 24 hours. FDG labeling of these cells was carried out as described in the previous section, including cell fasting and incubation with FDG for 1 hour (370 MBq/ml, 200 μl per well). We added 10 μl of CCK-8 reagent (Sigma-Aldrich, #96992) to each well at times 0, 6, 24, and 54 hours after radiolabeling. Cells incubated with methanol for 10 min were prepared as positive control samples. We measured the absorbance of the

solution at 450 nm using a plate reader (GloMax multi-detection system, Promega). The metabolism of radiolabeled cells was compared to control cells that were cultured similarly to the labeled cells in all aspects but were not labeled with FDG.

We also used the Sytox Green dye to assess the integrity of the cell membrane immediately after radiolabeling. While performing the radiolabeling procedure mentioned in the previous section, we added 2 μl of Sytox Green dye (Thermo Fisher Scientific, NucGreen #R37109) to 500 μl of FDG-labeled B16 cell suspension for 15 min at room temperature. The excess dye was removed, and the Sytox-stained cells were quantified by flow cytometry using the single-cell sorter (Hana, Namocell). B16 cells fixed using ice-cold ethanol for 15 min were prepared as the positive control for this assay.

Apoptosis assay (annexin V staining)

Annexin V was used to measure apoptosis after radiolabeling. B16 cells were seeded into a six-well plate (2×10^5 cells per well) and cultured for 48 hours. The cells were then labeled with FDG as previously described. Excess FDG was removed, and the radiolabeled cells were stained with an annexin V staining kit (Abcam, #ab176749) 3 hours after radiolabeling. Annexin V–labeled cells were quantified by flow cytometry using a single-cell sorter (Hana, Namocell). B16 cells treated with cisplatin (100 μM; Sigma-Aldrich, #P4394) for 48 hours were prepared as a positive control for this assay.

Lipid peroxidation characterization

The lipid peroxidation sensor BODIPY 581/591 C11 (Invitrogen, #D3861) was used to characterize the peroxidation of lipid membranes in FDG-labeled cells. As a comparison, we also characterized untreated cells (negative control), cells irradiated with 10- and 20-Gy x-ray radiation [320 kilovolt peak (kVp) and 12.5 mA; X-RAD 320; Precision X-Ray Inc.], and cells treated with cumene hydroperoxide (200 μM for 2 hours; positive control). The probe BODIPY 581/591 C11 targets cell membranes in live cells, and the oxidation of its polyunsaturated butadienyl portion triggers a shift in fluorescence emission peak from red (~590 nm) to green (~510 nm). Cells were stained before treatment with BODIPY C11 (5 μM) at room temperature for 30 min. The assay was readout by flow cytometry (Novocyte, Panteon) 2 hours after staining.

DNA damage assay (γH2AX staining)

We used γH2AX immunostaining to characterize DNA damage caused by radiolabeling. We first seeded 1.5×10^5 B16 cells into glass-bottom dishes (iBidi, #81218-200) and cultured them for 36 hours. Following the FDG labeling procedure, we stained FDG-labeled and control cells against γH2AX at 0 and 24 hours postlabeling. The immunostaining procedure started with fixing the cells in methanol on ice for 5 min, followed by cell permeabilization with 0.1% Triton X-100 in PBS for 10 min and blocking in 1% bovine serum albumin/0.1% Tween 20 in PBS for 30 min. The cells were then stained using a primary antibody against γH2AX (1:100 dilution; Sigma-Aldrich, #05-636) in the blocking solution at 4°C overnight. Secondary staining was carried out using an anti-mouse Alexa Fluor 488 antibody (1:100 dilution; Thermo Fisher Scientific, #A-21202) in PBS. The cell nuclei were stained with 4′,6-diamidino-2-phenylindole (1:50 dilution; Thermo Fisher Scientific, NucBlue #R37606) in PBS. As an additional reference, we irradiated cells (10 and 20 Gy) using x-ray (225 kV; 13 mA; X-RAD SmART irradiator, Precision X-Ray Inc.). These irradiated cells were stained 10 min following radiation, together with control unirradiated and labeled cells. Last, the stained cells were imaged using a fluorescence microscope (EVOS FL, 40× objective in oil), and mean fluorescence intensity was quantified using ImageJ software.

Cell migration assays

We used the wound healing assay to examine the ability of radiolabeled cells to proliferate and migrate in response to a mechanical scratch of the cell monolayer. We first seeded B16 cells into a six-well plate at 1.5×10^5 cells per well and cultured the cells for 36 hours. B16 cells were radiolabeled with FDG as described in the previous section, and then a gap of 0.8- to 1-mm width was created by scratching the cell monolayer with a narrow cell scratcher. The process of closing the gap was observed with a bright-field microscope (EVOS FL, 4× objective) at 0, 6, 24, and 48 hours after gap creation. B16 cells treated with cisplatin (100 μM; Sigma-Aldrich, #P4394) for 48 hours were prepared as the positive control for this assay.

Cell migration was further evaluated using Transwell permeable inserts equipped with 8.0-μm-pore polycarbonate membranes (Corning, NY, USA). B16 cells were labeled with FDG (370 MBq/ml) as previously described. They were then trypsinized, counted, and resuspended in serum-free DMEM to achieve a density of 7.5×10^5 cells/ml. A total of 300 μl of this cell suspension was placed in the upper chamber of the insert, while the lower chamber received 750 μl of DMEM supplemented with 10% FBS to serve as a chemoattractant. Cells not exposed to FDG served as negative control, while cells treated with 10% dimethyl sulfoxide served as a positive control. The assembled Transwell units were incubated for 48 hours at 37°C in a humidified atmosphere containing 5% CO_2, facilitating cell migration through the membrane pores. Postincubation, cells that did not migrate were gently removed from the upper surface of the membrane using a cotton swab. The cells on the lower surface that had migrated through the membrane were fixed with 4% paraformaldehyde for 15 min, stained with 0.2% crystal violet for 20 min, and subsequently rinsed with distilled water. Quantification was performed by counting stained cells across five randomly chosen fields under a light microscope (Leica, DMi8) at ×200 magnification. The migration potential was calculated and presented as the mean ± SD from three independent experiments.

Radiolabeling efflux

To examine the FDG efflux following radiolabeling, we seeded B16 cells onto a 96-well plate at a cell density of 15,000 cells per well and grew the cells for 24 hours. FDG labeling was performed per our standard protocol (370 MBq/ml, 200 μl per well). We removed excess FDG and washed the cells thrice with PBS (100 μl each time). We collected the supernatant and the lysed cells at times 0, 30, 60, 90, and 120 min after the removal of FDG. The radioactivity of these samples was measured with a gamma counter (Hidex). We characterized the efflux of FDG in three different culture media with different concentrations of D-glucose (0, 1.5, and 4.5 g/liter). The FDG retention percentage was computed as the ratio of the radioactivity in lysed cells over that in both lysed cells and the supernatant.

Intracellular and extracellular FDG metabolite characterization

We used instant thin-layer chromatography (iTLC) to analyze extracellular and intracellular FDG metabolites in radiolabeled B16 cells. After being labeled with FDG, the cells were incubated in complete

DMEM media for 90 min. To assess extracellular FDG metabolites, the supernatant was collected. Intracellular material was extracted using radioimmunoprecipitation assay lysis buffer and a cell scraper, followed by centrifugation at 14,000*g* for 15 min to remove cell debris. Both extracellular and intracellular samples were characterized by iTLC using acetonitrile/tetrabutylammonium hydroxide (10 mM per water; 8:1:1 volume ratio) as the mobile phase and silica gel–coated plastic sheets (Polygram SIL G/UV254; Macherey-Nagel) as the stationary phase, following a previously reported method (*45*). We applied 5 μl of the sample solutions onto a 2-cm strip and immersed it in a small beaker containing 10 ml of the mobile phase for 35 min. Following this, the strip was removed and air-dried, and the radioactivity profile was measured using an iTLC device (Lab Logic, Dual Scan-Ram).

Injection of radiolabeled single cells in vivo

All in vivo procedures in this study followed the protocol approved by the Administrative Panel on Laboratory Animal Care at Stanford University. We injected FDG-labeled single cells into athymic nude mice (*Foxn1*^{nu}, female, 6 to 8 weeks old, strain #490, Charles River), C57BL/6 mice (female, 6 to 8 weeks old, strain #027, Charles River), and BALB/c mice (female, 6 to 8 weeks old, strain #028, Charles River) via tail vein (intravenous) and left cardiac ventricle (intracardiac) routes. The mice were anesthetized using 2% isoflurane concentration and oxygen flow rate (0.5 liter/min) during the injection. The injection volume was 100 to 150 μl and contained around 40 FDG-labeled cells. We estimate that around half of the cells were successfully injected, whereas the other half was lost during transfer due to the dead volume of the syringe and adhesion to the microcentrifuge tube and micropipette tip. For intravenous injection, we first warmed the mouse tail with lukewarm water for 2 to 5 min until the tail vein became visible and then injected the cells using an insulin syringe (BD Biosciences) attached to a 28-g needle. For intracardiac injection, we used an ultrasound system (Vevo 2100, Visual Sonics) to guide the needle to the mouse's left ventricle in real time (*46*).

PET/CT imaging of radiolabeled single cells

We used a dual-layer BGO/LYSO PET/CT scanner (GNEXT, Sofie Biosciences) to image FDG-labeled single cells in vials and in vivo. Mice were anesthetized using 2% isoflurane and oxygen flow rate (0.5 liters/min) during imaging. PET images were acquired with an acquisition time of 10 min and the standard energy window (350 to 650 keV). CT images were acquired using the standard settings with a 2-min scan time and an 80-kVp beam energy. The PET images were reconstructed using the conventional OSEM method provided by the vendor with the scanner. We used the OsiriX software to view PET and CT images. Image display was achieved via maximum intensity projection of the PET data using a slice thickness of 6 mm for small vials and 21 to 22 mm for mice, which allowed us to display all the single cells in a single slice. To quantify the radioactivity of the single cells, we used the Inveon Research Workspace software to define spherical ROIs surrounding the cells and to calculate the activity per cell (obtained by multiplying ROI mean intensity by ROI volume).

PEPT-EM tracking algorithm

The PEPT-EM tracking algorithm was originally reported by Manger *et al.* (*26*) to track the 3D positions of chemical particles labeled with large amounts of radioactivity (>1 MBq). Briefly, the PEPT-EM algorithm uses a Gaussian-mixture model and maximum-likelihood expectation maximization to cluster the recorded photon coincidence events according to the estimated position of the cell from which they were most likely emitted. These coincidence events are recorded in list-mode format and are assigned a timestamp and an LOR (the line formed by two annihilation photons after positron combines with electron). The algorithm is iterative and alternates between clustering the list-mode data and estimating the new positions of the labeled cells until converging to the maximum-likelihood positions of these cells. Additional details of the PEPT-EM algorithm are provided in Supplementary Methods. The algorithm was implemented using MATLAB (version 2022).

To provide input to the PEPT-EM algorithm, we first had to convert the list-mode data from the machine-generated format to a format readable by MATLAB, validate this conversion method (fig. S22), optimize the annihilation photon penetration depth (fig. S23), and coregister the 3D positions produced by our algorithm with the reference frame of the GNEXT PET/CT (fig. S24). Additional details are provided in Supplementary Methods. In addition, the algorithm must be initialized by generating random cell positions. For experiments involving cells in vials, the initial positions were randomly generated within 25 mm of the vial location as seen on CT (movie S1). For in vivo experiments, the initial positions were randomized within the central region of each mouse (movie S4). The stopping criteria were set at a maximum of 300 iterations or a total change in the positions of the sources between consecutive iterations of 0.01 mm or less.

Injection, imaging, and segmentation of CT contrast agent

To enhance the visualization of the vasculature in the mouse model, we intravenously injected a CT contrast agent (ExiTron nano 12000; Miltenyi Biotec) into some of the mice. We used the highest-resolution settings on the Sofie GNEXT (80 kVp; bin 1; 100-μm voxels) to acquire CT images of the mice 15 min after the injection of the CT contrast agent. The CT images were then fused with the matching PET images and displayed using 3D Slicer software. Segmentation of the cardiovascular and bony anatomy was done using ITK-SNAP, which is a semi-automatic threshold-based toolkit (*47*). Most segmentation algorithms require initialization points, followed by setting a singular value to begin the threshold-based region growth. We opted to use Otsu's multithreshold method to select a specific value based on the current region of interest. Then, the ITK-SNAP region growth algorithm was used to grow the segment from the previous segment. For the vessels, the threshold was approximately 147 to 325 Hounsfield units, while for the bone, a lower threshold of 450 to 670 Hounsfield units was used. Last, we also conducted a short longitudinal experiment to observe the kinetics of the contrast agent accumulation in the vasculature and various other organs at 15, 30, and 24 hours postinjection.

Locating single cells after intracardiac injection

We examined six mice that were successfully administered with FDG-labeled cells via intracardiac injection (successful rate, ~30%). In these mice, we could visualize radiolabeled cells spreading to multiple organs throughout the body. The number of injected cells in each mouse varied from 5 to 40 cells, with a total of 74 cells that could be detected in six mice. The anatomical locations of the arrested cells within the body were determined by a board-certified orthopedic surgeon (coauthor Y.W.) by inspecting the PET/CT data using the OsiriX software.

Ex vivo validation

Additional ex vivo imaging studies were conducted to confirm the exact localization of single cancer cells after injection into mice. B16 cancer cells were dual-labeled with FDG and DiO, a fluorescent dye. After injection and imaging, the mice were euthanized, and the major organs were excised and imaged ex vivo using PET/CT. Guided by these images, we narrowed the location of the single cells down to a smaller piece of tissue, about 1- to 2-mm thick, which we dissected for further optical imaging. Gamma counting was used to confirm the presence of radioactivity in these tissues. The tissues were then made optically clear using the Ce3D protocol (room temperature, 6 hours), as previously described (*48*). The optically cleared tissues were imaged with a Leica M205 Stereo Fluorescence Microscope to verify the fluorescence of the cancer cells within the excised tissues. DiO labeling was performed right after FDG labeling for 15 min at 37°C with a 10 μM concentration.

Statistical analysis

All analyses comparing differences between groups in this study were conducted with R (Rstudio 2018) via analysis of variance (ANOVA) combined with the Tukey test as a post hoc analysis. The notions of significant differences are as follows: $*P < 0.05$, $**P < 0.01$, $***P < 0.001$, and $****P < 0.0001$.

Code availability

The MATLAB code used to track single cells via the PEPT-EM algorithm and the code to import raw list-mode PET data into MATLAB are publicly available on Dryad https://doi.org/10.5061/dryad.3bk3j9kt4.

Supplementary Materials

This PDF file includes:

Figs. S1 to S29
Supplementary Methods
Legends for movies S1 to S6

Other Supplementary Material for this manuscript includes the following:

Movies S1 to S6

REFERENCES AND NOTES

1. H. Hong, Y. Yang, Y. Zhang, W. Cai, Non-invasive cell tracking in cancer and cancer therapy. *Curr. Top. Med. Chem.* **10**, 1237–1248 (2010).
2. L. Ottobrini, C. Martelli, D. L. Trabattoni, M. Clerici, G. Lucignani, In vivo imaging of immune cell trafficking in cancer. *Eur. J. Nucl. Med. Mol. Imaging* **38**, 949–968 (2011).
3. C. Lauri, M. Varani, V. Bentivoglio, G. Capriotti, A. Signore, Present status and future trends in molecular imaging of lymphocytes. *Semin. Nucl. Med.* **53**, 125–134 (2023).
4. F. A. Oliveira, M. P. Nucci, I. S. Filgueiras, J. M. Ferreira, L. P. Nucci, J. B. Mamani, F. Alvieri, L. E. B. Souza, G. N. A. Rego, A. T. Kondo, N. Hamerschlak, L. F. Gamarra, Noninvasive tracking of hematopoietic stem cells in a bone marrow transplant model. *Cells* **9**, 939 (2020).
5. D. J. Laird, U. H. von Andrian, A. J. Wagers, Stem cell trafficking in tissue development, growth, and disease. *Cell* **132**, 612–630 (2008).
6. X. Wang, M. Rosol, S. Ge, D. Peterson, G. McNamara, H. Pollack, D. B. Kohn, M. D. Nelson, G. M. Crooks, Dynamic tracking of human hematopoietic stem cell engraftment using in vivo bioluminescence imaging. *Blood* **102**, 3478–3482 (2003).
7. J. D. Amack, Cellular dynamics of EMT: Lessons from live in vivo imaging of embryonic development. *Cell Commun. Signal.* **19**, 79 (2021).
8. X. Yuan, X. Yu, B. Dai, Z. Zhang, Advances in intravital imaging of liver immunity using optical microscopy and labeling methods. *iRADIOLOGY* **1**, 61–77 (2023).
9. L. M. Lechermann, D. Lau, B. Attili, L. Aloj, F. A. Gallagher, In vivo cell tracking using PET: Opportunities and challenges for clinical translation in oncology. *Cancers* **13**, 4042 (2021).
10. R. Pfeifer, J. Henze, K. Wittich, A. Gosselink, A. Kinkhabwala, F. Gremse, C. Bleilevens, K. Bigott, M. Jungblut, O. Hardt, F. Alves, W. Al Rawashdeh, A multimodal imaging workflow for monitoring CAR T cell therapy against solid tumor from whole-body to single-cell level. *Theranostics* **12**, 4834–4850 (2022).
11. S. Harmsen, E. I. Medine, M. Moroz, F. Nurili, J. Lobo, Y. Dong, M. Turkekul, N. V. K. Pillarsetty, R. Ting, V. Ponomarev, O. Akin, O. Aras, A dual-modal PET/near infrared fluorescent nanotag for long-term immune cell tracking. *Biomaterials* **269**, 120630 (2021).
12. K. O. Jung, T. J. Kim, J. H. Yu, S. Rhee, W. Zhao, B. Ha, K. Red-Horse, S. S. Gambhir, G. Pratx, Whole-body tracking of single cells via positron emission tomography. *Nat. Biomed. Eng.* **4**, 835–844 (2020).
13. K. S. Lee, T. J. Kim, G. Pratx, Single-cell tracking with PET using a novel trajectory reconstruction algorithm. *IEEE Trans. Med. Imaging* **34**, 994–1003 (2015).
14. Y. Ouyang, T. J. Kim, G. Pratx, Evaluation of a BGO-based PET system for single-cell tracking performance by simulation and phantom studies. *Mol. Imaging* **15**, 153601211664648 (2016).
15. Z. Gu, D. L. Prout, R. W. Silverman, H. Herman, A. Dooraghi, A. F. Chatziioannou, A DOI detector with crystal scatter identification capability for high sensitivity and high spatial resolution PET imaging. *IEEE Trans. Nucl. Sci.* **62**, 740–747 (2015).
16. Z. Gu, R. Taschereau, N. T. Vu, D. L. Prout, J. Lee, A. F. Chatziioannou, Performance evaluation of HiPET, a high sensitivity and high resolution preclinical PET tomograph. *Phys. Med. Biol.* **65**, 045009 (2020).
17. H. Alva-Sánchez, A. Zepeda-Barrios, V. D. Díaz-Martínez, T. Murrieta-Rodríguez, A. Martínez-Dávalos, M. Rodríguez-Villafuerte, Understanding the intrinsic radioactivity energy spectrum from ^{176}Lu in LYSO/LSO scintillation crystals. *Sci. Rep.* **8**, 17310 (2018).
18. M. Conti, L. Eriksson, H. Rothfuss, T. Sjoeholm, D. Townsend, G. Rosenqvist, T. Carlier, Characterization of ^{176}Lu background in LSO-based PET scanners. *Phys. Med. Biol.* **62**, 3700–3711 (2017).
19. W. Shi, "Radiation therapy for melanoma" in *Cutaneous Melanoma: Etiology and Therapy*, W. H. Ward, J. M. Farma, Eds. (Codon Publications, 2017), pp. 101–120.
20. F. E. Langlands, K. Horgan, D. D. Dodwell, L. Smith, Breast cancer subtypes: Response to radiotherapy and potential radiosensitisation. *Br. J. Radiol.* **86**, 20120601 (2013).
21. S. A. Graves, R. T. Flynn, D. E. Hyer, Dose point kernels for 2,174 radionuclides. *Med. Phys.* **46**, 5284–5293 (2019).
22. A. M. Barron, E. R. Rosario, R. Elteriefi, C. J. Pike, Sex-specific effects of high fat diet on indices of metabolic syndrome in 3xTg-AD mice: Implications for Alzheimer's disease. *PLOS ONE* **8**, e78554 (2013).
23. C. R. K. Windows-Yule, J. P. K. Seville, A. Ingram, D. J. Parker, Positron emission particle tracking of granular flows. *Annu. Rev. Chem. Biomol. Eng.* **11**, 367–396 (2020).
24. C. R. K. Windows-Yule, M. T. Herald, A. L. Nicuşan, C. S. Wiggins, G. Pratx, S. Manger, A. E. Odo, T. Leadbeater, J. Pellico, R. T. M. de Rosales, A. Renaud, I. Govender, L. B. Carasik, A. E. Ruggles, T. Kokalova-Wheldon, J. P. K. Seville, D. J. Parker, Recent advances in positron emission particle tracking: A comparative review. *Rep. Prog. Phys.* **85**, 016101 (2022).
25. A. L. Nicuşan, C. R. K. Windows-Yule, Positron emission particle tracking using machine learning. *Rev. Sci. Instrum.* **91**, 013329 (2020).
26. S. Manger, A. Renaud, J. Vanneste, An expectation–maximization algorithm for positron emission particle tracking. *Rev. Sci. Instrum.* **92**, 085102 (2021).
27. S. Pal, D. S. Perrien, T. Yumoto, R. Faccio, A. Stoica, J. Adams, C. M. Coopersmith, R. M. Jones, M. N. Weitzmann, R. Pacifici, The microbiome restrains melanoma bone growth by promoting intestinal NK and Th1 cell homing to bone. *J. Clin. Invest.* **132**, e157340 (2022).
28. J. P. Campbell, A. R. Merkel, S. K. Masood-Campbell, F. Elefteriou, J. A. Sterling, Models of bone metastasis. *J. Vis. Exp.*, e4260 (2012).
29. L. Gómez-Cuadrado, N. Tracey, R. Ma, B. Qian, V. G. Brunton, Mouse models of metastasis: Progress and prospects. *Dis. Model. Mech.* **10**, 1061–1074 (2017).
30. F. Arguello, R. B. Baggs, C. N. Frantz, A murine model of experimental metastasis to bone and bone marrow. *Cancer Res.* **48**, 6876–6881 (1988).
31. T. Kuchimaru, N. Kataoka, K. Nakagawa, T. Isozaki, H. Miyabara, M. Minegishi, T. Kadonosono, S. Kizaka-Kondoh, A reliable murine model of bone metastasis by injecting cancer cells through caudal arteries. *Nat. Commun.* **9**, 2981 (2018).
32. D. D. Nolting, M. L. Nickels, N. Guo, W. Pham, Molecular imaging probe development: A chemistry perspective. *Am. J. Nucl. Med. Mol. Imaging* **2**, 273–306 (2012).
33. H. A. Lehr, M. Leunig, M. D. Menger, D. Nolte, K. Messmer, Dorsal skinfold chamber technique for intravital microscopy in nude mice. *Am. J. Pathol.* **143**, 1055–1062 (1993).
34. M. Cazaux, C. L. Grandjean, F. Lemaître, Z. Garcia, R. J. Beck, I. Milo, J. Postat, J. B. Beltman, E. J. Cheadle, P. Bousso, Single-cell imaging of CAR T cell activity in vivo reveals extensive functional and anatomical heterogeneity. *J. Exp. Med.* **216**, 1038–1049 (2019).
35. S. Iwano, M. Sugiyama, H. Hama, A. Watakabe, N. Hasegawa, T. Kuchimaru, K. Z. Tanaka, M. Takahashi, Y. Ishida, J. Hata, S. Shimozono, K. Namiki, T. Fukano, M. Kiyama, H. Okano, S. Kizaka-Kondoh, T. J. McHugh, T. Yamamori, H. Hioki, S. Maki, A. Miyawaki, Single-cell bioluminescence imaging of deep tissue in freely moving animals. *Science* **359**, 935–939 (2018).
36. M. Masthoff, F. N. Freppon, L. Zondler, E. Wilken, L. Wachsmuth, S. Niemann, C. Schwarz, I. Fredrich, A. Havlas, H. Block, M. Gerwing, A. Helfen, W. Heindel, A. Zarbock, M. Wildgruber, C. Faber, Resolving immune cells with patrolling behaviour by magnetic resonance time-lapse single cell tracking. *EBioMedicine* **73**, 103670 (2021).

37. C. Heyn, J. A. Ronald, S. S. Ramadan, J. A. Snir, A. M. Barry, L. T. MacKenzie, D. J. Mikulis, D. Palmieri, J. L. Bronder, P. S. Steeg, T. Yoneda, I. C. MacDonald, A. F. Chambers, B. K. Rutt, P. J. Foster, In vivo MRI of cancer cell fate at the single-cell level in a mouse model of breast cancer metastasis to the brain. *Magn. Reson. Med.* **56**, 1001–1010 (2006).
38. L. Kiru, A. Zlitni, A. M. Tousley, G. N. Dalton, W. Wu, F. Lafortune, A. Liu, K. M. Cunanan, H. Nejadnik, T. Sulchek, M. E. Moseley, R. G. Majzner, H. E. Daldrup-Link, In vivo imaging of nanoparticle-labeled CAR T cells. *Proc. Natl. Acad. Sci. U.S.A.* **119**, e2102363119 (2022).
39. S. Paget, The distribution of secondary growths in cancer of the breast. *Lancet* **133**, 571–573 (1889).
40. R. R. Langley, I. J. Fidler, The seed and soil hypothesis revisited—The role of tumor-stroma interactions in metastasis to different organs. *Int. J. Cancer* **128**, 2527–2535 (2011).
41. P. J. Muire, L. H. Mangum, J. C. Wenke, Time course of immune response and immunomodulation during normal and delayed healing of musculoskeletal wounds. *Front. Immunol.* **11**, 1056 (2020).
42. K. O. Jung, A. J. Theruvath, H. Nejadnik, A. Liu, L. Xing, T. Sulchek, H. E. Daldrup-Link, G. Pratx, Mechanoporation enables rapid and efficient radiolabeling of stem cells for PET imaging. *Sci. Rep.* **12**, 2955 (2022).
43. A. Liu, M. Islam, N. Stone, V. Varadarajan, J. Jeong, S. Bowie, P. Qiu, E. K. Waller, A. Alexeev, T. Sulchek, Microfluidic generation of transient cell volume exchange for convectively driven intracellular delivery of large macromolecules. *Mater. Today* **21**, 703–712 (2018).
44. H. Nejadnik, K. O. Jung, A. J. Theruvath, L. Kiru, A. Liu, W. Wu, T. Sulchek, G. Pratx, H. E. Daldrup-Link, Instant labeling of therapeutic cells for multimodality imaging. *Theranostics* **10**, 6024–6034 (2020).
45. M. Simone, P. Olaf, H. Markus, J. T. Deichen, K. Torsten, Characterization of 18F-FDG uptake in human endothelial cells in vitro. *J. Nucl. Med.* **45**, 455 (2004).
46. Y.-Q. Zhou, L. Davidson, R. M. Henkelman, B. J. Nieman, F. S. Foster, L. X. Yu, X. J. Chen, Ultrasound-guided left-ventricular catheterization: A novel method of whole mouse perfusion for microimaging. *Lab. Invest.* **84**, 385–389 (2004).
47. P. A. Yushkevich, J. Piven, H. C. Hazlett, R. G. Smith, S. Ho, J. C. Gee, G. Gerig, User-guided 3D active contour segmentation of anatomical structures: Significantly improved efficiency and reliability. *Neuroimage* **31**, 1116–1128 (2006).
48. W. Li, R. N. Germain, M. Y. Gerner, High-dimensional cell-level analysis of tissues with Ce3D multiplex volume imaging. *Nat. Protoc.* **14**, 1708–1733 (2019).

Acknowledgments: We sincerely appreciate the fruitful discussion with Stanford Professor H. Song on intracardiac injection and N. Vu (Sofie Company) on converting raw data from the GNext PET scanner to LOR data. We would like to thank Stanford SCI^3 Directors F. Habte and L. J. Pisani for providing support with molecular imaging equipment used in this study. We are truly thankful to the Stanford Cyclotron and Radiochemistry Facility Director, the late B. Shen, and technicians F. Balmaceda and K. Ho for help with FDG orders and Namocell employees (J. Lin and T. Lu) for assisting with single-cell dispensing. Figure 1 was created in part with BioRender.com. **Funding:** Research reported in this publication was supported by the National Institute of Biomedical Imaging and Bioengineering of the National Institutes of Health under Award Number R01EB030367 (awarded to G.P.). The content is solely the responsibility of the authors and does not necessarily represent the official views of the National Institutes of Health. H.T.M.N. gratefully acknowledges funding through the Stanford School of Medicine Dean's Postdoctoral Fellowship, the Stanford Radiation Oncology and Medical Physics Trainee Seed Grant, and the NIH Stanford Molecular Imaging Scholars (SMIS) Program (NCI T32CA118681). **Author contributions:** G.P. contributed to the conceptualization, experiment design, resources, and editing of the manuscript; C.K.F.C. contributed resources; E.R. contributed resources; N.D. contributed to experiments (intracardiac injections and Transwell assay); M.R. contributed to analysis (MC simulations); X.Z. contributed to analysis (radiation dose calculation); E.T. contributed to experiments (ex vivo validation); Y.W. contributed to analysis (single-cell distribution after intracardiac injection); C.R. and B.M. contributed to analysis (CT segmentation); H.T.M.N. contributed to conceptualization, experiment design, experiments, analysis, and manuscript writing. **Competing interests:** The authors declare that they have no competing interests. **Data and materials availability:** All data needed to evaluate the conclusions in the paper are present in the paper and/or the Supplementary Materials. The PET/CT images (DICOM) showing FDG-labeled single cells in vivo have been uploaded to the Dryad repository, accessible via https://doi.org/10.5061/dryad.3bk3j9kt4.

Submitted 30 August 2023
Accepted 13 May 2024
Published 14 June 2024
10.1126/sciadv.adk5747